

Atomic Force Microscopy Detects the Difference in Cancer Cells of Different Neoplastic Aggressiveness via Machine Learning

Siona Prasad, Alex Rankine, Tarun Prasad, Patrick Song, Maxim E. Dokukin, Nadezda Makarova, Vadim Backman, and Igor Sokolov*

A novel method based on atomic force microscopy (AFM) working in Ringing mode (RM) to distinguish between two similar human colon epithelial cancer cell lines that exhibit different degrees of neoplastic aggressiveness is reported on. The classification accuracy in identifying the cell line based on the images of a single cell can be as high as 94% (the area under the receiver operating characteristic [ROC] curve is 0.99). Comparing the accuracy using the RM and the regular imaging channels, it is seen that the RM channels are responsible for the high accuracy. The cells are also studied with a traditional AFM indentation method, which gives information about cell mechanics and the pericellular coat. Although a statistically significant difference between the two cell lines is also seen in the indentation method, it provides the accuracy of identifying the cell line at the single-cell level less than 68% (the area under the ROC curve is 0.73). Thus, AFM cell imaging is substantially more accurate in identifying the cell phenotype than the traditional AFM indentation method. All the obtained cell data are collected on fixed cells and analyzed using machine learning methods. The biophysical reasons for the observed classification are discussed.

1. Introduction

Atomic force microscopy (AFM) is a technique that allows visualizing surfaces down to the nanoscale. Beyond pure microscopy, AFM can be used to measure the mechanical properties of samples, in particular, biological cells.^[1,2] Further development of AFM modes has shown that the AFM technique can also be used to obtain information about the pericellular layer, a layer of molecules grafted to the pericellular membrane surrounding cells.^[3-5] All this wealth of information can be used to address important medical questions, for example, the problems of cancer detection. There is a host of works reporting the differences in the mechanical properties of cancer and normal cells,^[6,7] cancer cells of different metastatic activity,^[4,5,8] and even cancer-initiating cells.^[9] It was also found that cancer cells of different aggressiveness have a substantially different pericellular coat, a layer of molecules grafted to the pericellular membrane surrounding cells.^[3-5] The challenge of using these properties to identify the cell

S. Prasad, A. Rankine, T. Prasad, P. Song, N. Makarova, Prof. I. Sokolov
Department of Mechanical Engineering
Tufts University
Medford, MA 02155, USA
E-mail: Igor.Sokolov@Tufts.edu

S. Prasad, A. Rankine, T. Prasad, P. Song
Department of Computer Science
Harvard University
Cambridge, MA 02138, USA

Dr. M. E. Dokukin
NanoScience Solutions, Inc
Arlington, VA 22203, USA

 The ORCID identification number(s) for the author(s) of this article can be found under <https://doi.org/10.1002/anbr.202000116>.

© 2021 The Authors. Advanced NanoBiomed Research published by Wiley-VCH GmbH. This is an open access article under the terms of the Creative Commons Attribution License, which permits use, distribution and reproduction in any medium, provided the original work is properly cited.

DOI: 10.1002/anbr.202000116

Dr. M. E. Dokukin
Department of Information Technology and Electronics
Sarov Physics and Technology Institute
Sarov, Russian Federation

Dr. M. E. Dokukin
Institute of Nanoengineering in Electronics, Spintronics and Photonics
National Research Nuclear University MEPhI
Moscow, Russian Federation

Prof. V. Backman
Department of Biomedical Engineering
Northwestern University
Evanston, IL 60208, USA

Prof. I. Sokolov
Department of Biomedical Engineering
Tufts University
Medford, MA 02155, USA

Prof. I. Sokolov
Department of Physics
Tufts University
Medford, MA 02155, USA

phenotype lies in the difficulty of controlling cell physical properties during sample preparation. It was shown, for example, that the elastic modulus and pericellular coat of cells can change during sample preparation substantially more than the difference between cancer and normal cells.^[10] Furthermore, the accuracy of detection based on mechanical properties typically requires to analyze a substantial number of cells, which is time-consuming when using AFM. In addition, living cells are considered to be biohazard, which may complicate their handling in a diagnostic lab environment.

To overcome the aforementioned problems, it was suggested to use fixed cells.^[11,12] A special method of fixation was developed to protect the fine structure of the cell surface.^[12,13] The approach was demonstrated on the example of human cervical epithelial cells.^[11,12,14] It was shown that the AFM imaging of fixed cells is capable of detecting all stages of progression toward cancer. Interestingly, it was possible to do this by using a single surface parameter, fractal dimension (and later, multifractality), which was calculated using the maps of adhesion.^[12,14,15] However, the use of a single parameter had a serious limitation. While it was possible to segregate each cancer and normal cells unambiguously, it was impossible to find such a precise separation between precancerous and cancerous cells. Moreover, a recent study using exfoliated bladder cells extracted from urine has shown that single surface parameters do not work for separations of cells obtained from patients with and without active bladder cancer.^[16] The problem was successfully addressed through the use of machine learning analysis, which allows taking into consideration multiple surface parameters, which are typically used in engineering to describe sample surface (e.g., roughness, see previous studies^[11,12,14,16] for more details). It was shown that the AFM imaging of the adhesion maps of cells extracted from urine could be used to detect active bladder cancer with an accuracy of 94% (when using five cells per patient to make the diagnosis).

In the current work, we apply machine learning to test the hypothesis that AFM imaging of fixed cells can be used to differentiate cancer cells of different neoplastic behavior. This problem is significant because at present there is no accepted method to identify the degree of malignancy at the level of single cells. Solving this problem will help doctors to prescribe the efficient treatment early, thereby decreasing the mortality of cancer.^[17-19]

Here, we presented the study of two similar but genetically altered human colon cancer cell lines, HT29 cells, and Csk cells.^[20,21] The latter are shRNA-transfected HT29 cells that exhibit different degrees of neoplastic aggressiveness. It is a more proliferative phenotype compared with HT29 cells. Here, we study cells using both AFM methods, the traditional study of cell mechanics (including the pericellular coat) and the AFM imaging of the cell surface. The data contained in AFM images were then reduced to a set of surface parameters mentioned earlier. The obtained information was further processed by means of a machine learning algorithm.

In addition to the previous AFM imaging, here we utilized a recently introduced multidimensional AFM modality, Ringing mode (RM),^[22-24] which allows recording the images of the distribution of several physical properties of the sample surface. Specifically, together with the standard height and adhesion channels, we recorded three additional imaging channels, RM restored adhesion, RM adhesion, and RM viscoelastic adhesion.

These five channels simultaneously recorded provide multidimensional images of the cell surface. We consider each channel/dimension separately for cell classification. It allows us to understand the power of each channel in the identification of the cell phenotype. In addition, we also combined all channels to enhance the segregation power of the method.

In the current work, we demonstrate that the regular approach of studying cell mechanics can also differentiate between the average values of these two cell lines. These differences were found in all three physical parameters extracted from the AFM indentation of cells (the Young's modulus, equilibrium length of the pericellular coat, and the effective grafting density of the pericellular coat molecules). However, these three parameters are not capable of differentiating each cell with sufficiently high accuracy. When combining all three physical parameters, the accuracy of identification of the cell line is only 68% (the area under the receiver operating characteristic curve [AUC ROC] is 0.73). In contrast, the machine learning algorithm working with the surface parameters is capable of differentiating individual HT29 and Csk cells with an accuracy of up to 94% (the AUC ROC is 0.99). We further calculate the full statistical characteristics of the obtained cell classification and demonstrate that the obtained results are robust.

To the best of our knowledge, the obtained accuracy is better than the accuracy of a single-cell DNA sequencing (which is not exceeding 80%^[25]) and close to single-cell RNA sequencing methods (accuracy $\approx 96\%$ ^[26-28]). It is definitely premature to compare the well-established single RNA and DNA sequencing with the results of this study. Nevertheless, we hope that our work shows the potential and will spark the interest of the research community to a broader investigation and utilization of the described method.

Because of the novelty of the described methods, we devote several next sections to the description of the method of AFM imaging, the data processing of AFM indentation of cells, and machine learning analysis of the obtained data. The results of the measurements and data processing are presented in Section 4. The traditional parts of the used methods are presented in the Experimental Section at the end.

2. AFM in Studying Cells

2.1. AFM Imaging of Cells in RM

RM is a relatively new imaging modality, which allows to obtain maps of physical properties of sample surfaces with higher resolution and speed compared with the more traditional subresonance tapping.^[22-24] It is based on advanced processing of the dynamic response of the cantilever (ringing) after disconnecting the AFM probe from the sample surface. RM used in this work was implemented as an expansion of PeakForce tapping, which is a subresonance imaging mode. In the previous work,^[16] the maps of adhesion of PeakForce tapping were used to identify cells extracted from urine of patients with active bladder cancer. (The adhesion stands for the pull off force between the AFM cantilever and cell surface.) Therefore, here we collect the adhesion images of cells as well as traditional height images when AFM working in the PeakForce tapping.

In addition to these two imaging channels, we record three RM channels: RM adhesion, RM restored adhesion, and RM viscoelastic adhesion. The difference between adhesion and RM adhesion is due to the difference in processing the AFM signal. The signal used for calculation of the RM adhesion was just minimally filtered to keep the value of the adhesion force unchanged (compared with the adhesion measured independently by the force-volume mode^[29]). When applied to fixed cells, the resolution of this method is of the order of 1 nm.^[16] The meaning of the RM restored adhesion is explained in detail in previous studies.^[22,23] Briefly, it is the force of adhesion between the AFM probe and cell surface at the moment of disconnection with the last part of the cell (e.g., molecules of the glycocalyx, which are pulled off by the action of the AFM probe while disconnecting). RM viscoelastic adhesion is essential in the difference between RM adhesion and RM restored adhesion. It is used here because of two reasons: 1) it has a definite physical sense (the force difference needed to stretch the surface molecules from the cell surface by the action of the AFM probe during detachment from the cell surface), and 2) it is instructive to verify if a simple linear combination of two channels would result in a better classification of cell phenotype; see Section 5 for detail.

To summarize, five imaging channels were recorded in this study: the height, adhesion (both channels are native of PeakForce QNM), and three novel RM channels: RM adhesion, RM restored adhesion, and RM viscoelastic adhesion. It is worth noting that all these imaging channels are recorded simultaneously.

2.2. AFM Method of Indentation of Cells; the Brush Model

The brush model is used to obtain information about mechanical properties of cell body and its pericellular coat (brush).^[30] To avoid collapsing of the brush layer, the measurements have to be done in aqueous environment. AFM indentation method is a traditional way to study the difference between various cancer cell lines. In this mode, the AFM probe is ramping up and down, measuring the force response of the probe that indents a cell. For precise measurements, it is important to know the geometry of the cell under the indenting probe. It is done with the help of force-volume mode.^[29] To find the mechanical properties of cells, the elastic modulus, and the properties of its pericellular coat, we used the AFM method called the brush model. This model was suggested in the study by Sokolov et al.,^[30] and later developed in previous studies.^[9,31,32] As was shown, considering the pericellular layer and the use of a large colloidal probe are essential for self-consistency of the Hertz model, which is used to extract the effective Young's modulus of the cell body (note that the Hertz model is used because there is no adhesion between the AFM probe and cell surface measured in liquids). This model is described in detail in the references mentioned earlier and recently overviewed.^[31] Briefly, a geometry of a spherical AFM probe deforming a cell body, which is covered with molecules of the pericellular coat, is shown in **Figure 1**. A geometrical reasoning provides the following relation between the geometrical parameters defined in the figure:

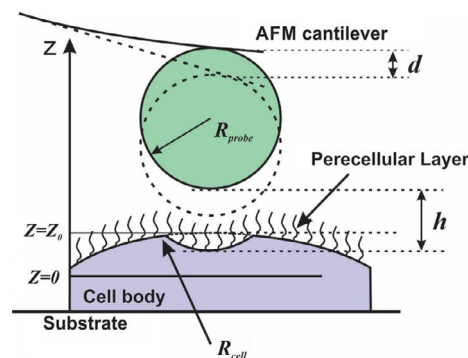


Figure 1. A schematic of AFM cantilever deforming the cell body covered with a molecular pericellular coat.

$$h = Z - Z_0 + \left[\frac{9k}{16E} \sqrt{\frac{R_{\text{probe}} + R_{\text{cell}}}{R_{\text{probe}} R_{\text{cell}}}} \right]^{2/3} d^{2/3} + d \quad (1)$$

where Z_0 is the position of the undeformed cell body, h is the distance between the AFM probe and the surface of the cell body, E is the elastic (Young's) modulus, k is the spring constant of the AFM cantilever, and R_{probe} (R_{cell}) are the radius of the AFM probe (cell). The Poisson ratio of a cell is chosen to be 0.5 (because of a small range of possible variations of ν , the error in the modulus due to the uncertainty of its definition is small, within 5%^[2]).

The experimental data are fitted with Equation (1) in two steps. In step 1, the indentation part corresponding to a relatively high force is considered (typically >3–5 nN for the case of epithelial cells). It is assumed that the soft pericellular layer is almost entirely squeezed at those forces, and consequently, $h = 0$ in Equation (1). This allows to use Equation (1) to extract the effective Young's modulus of the cell body. The assumption of squeezed pericellular layer is verified by independence of the Young's modulus on the indentation depth. This is, however, true only for a limited range of forces; for higher forces, the cell body cannot longer be treated as a homogeneous and isotropic material, as well as the substrate effect might be needed to be taken into account.

In step 2, Equation (1) is used to extract the force due to the pericellular layer. This is done by using the indentation data for forces smaller than the one needed to squeeze the brush layer. This pericellular brush layer can be characterized with two parameters: N is the surface density of the brush constituents (grafting density, or effective molecular density) and L is the equilibrium thickness of the brush layer. It can be found using the following equation (Alexander–de Gennes model), which is used for the force of repulsion between a spherical probe of radius R_{probe} and a semispherical cell of radius R_{cell} ^[33–35]

$$F(h) \approx 100k_B T R^* N^{3/2} \exp\left(-2\pi \frac{h}{L}\right) L \quad (2)$$

where k_B is the Boltzmann constant, T is the temperature, and $R^* = R_{\text{probe}} \times R_{\text{cell}} / (R_{\text{probe}} + R_{\text{cell}})$.

In this work, the AFM indentation measurements will be reduced to three parameters: the effective Young's modulus (E), equilibrium size of the pericellular coat (L), and the grafting density of the pericellular brush (N).

3. Data Processing Using Machine Learning Methods

In the described method, AFM images of cells are classified using the machine learning method, as shown in **Figure 2**. Five different AFM images were collected simultaneously for each cell. As AFM is a relatively slow technique, it is unrealistic to collect a large number of cell images. According to “the rule of ten,”^[36] the number of instances used for regression in machine learning methods should be at least ten times larger than the number of features used for the regression or classification. It means that the number of different cell images should be at least ten times larger than the number of features used for quantification of each image. If we used information of the entire image, 512×512 pixels, it would be totally unrealistic to obtain such a large number of AFM images. Although the rule of ten is not a rigid rule but rather a recommendation, it is paramount to reduce the dimension of the data space a substantially lower number of features.

To reduce the dimension of data space, we follow^[16] and use the so-called surface parameters as features to characterize each AFM image. The surface parameters are routinely used in multiple engineering applications to characterize surfaces, including cell surfaces.^[11,12,14,16] A complete list of parameters used in this work can be found in standards ISO 4287/1 ASME B46.1; ISO/DIS 25178-2. The surface parameters can be calculated by using a number of available software. For example, SPIP (by Image Metrology A/S, Denmark) can be used to calculate all surface parameters for 3D image surface arrays recorded by AFM. We used a home-built Python code to calculate these parameters and subsequently modify them by normalizing each of the parameters by the surface area (to the appropriate power) to make the surface parameters independent of the area of the images. This is important, as explained in the next paragraph. A good number of the parameters is already surface independent. Only the following parameters were modified to make them surface independent: S_{3a} , S_{td} , S_{tdi} , S_{rw} , S_{rwi} , S_{hw} , S_{cl} , and

S_{tr} . Several parameters did not carry relevant information (e.g., the image area, S_{2a}). As a result, each channel was effectively characterized with 35 surface parameters (the list of the surface parameters and examples of formulas used to calculate the parameters are given in the Supporting Information).

To calculate the surface parameters, each $10 \times 10 \mu\text{m}^2$ cell image was split typically in four equal zoomed images of $5 \times 5 \mu\text{m}^2$. Because of the specifics of the sample, it is impractical to prepare cell samples without any contamination on its surface. In principle, these artifacts could be identified automatically. But in the current work, we identify artifacts visually. Several examples of the artifacts in the cell images are shown in the Supporting Information (Figure S1–S3, Supporting Information; one can see abnormal horizontal lines in the images which are characteristic of the artifacts). The images with artifacts were not used for further processing. In some cases, it was difficult to find a $5 \times 5 \mu\text{m}^2$ area without artifacts. In such cases, we used a higher zoom to a smaller area. Therefore, it is important to use the modified surface parameters, which are surface independent, as described earlier.

The values of each pixel of the AFM images were used as is with the exception of the height image. This exception is because the absolute value of height in the AFM image does not carry any useful physical meaning. Second, we assume that the overall tilt of the cell surface does not carry any useful information either. Thus, each height image was preprocessed by removing a plane fitted using the least square method. This option is available in almost any AFM processing software (we used the SPIP software).

For the purpose of cell classification, we treated each AFM imaging channel independently. We also considered four channels combined to enhance the classification by making a plausible assumption that the combination of channels carries more information than each channel separately. The combination of four channels included all five channels with the exception of the adhesion channel. The adhesion channel presented too many artifacts, and consequently, keeping this channel in combination with others would substantially reduce the number of cells which can be considered for the subsequent analysis.

In the next step, we further reduced the number of the used surface parameters by using the Gini index ranking of the parameters features by their power in cell classification.^[37] By taking a

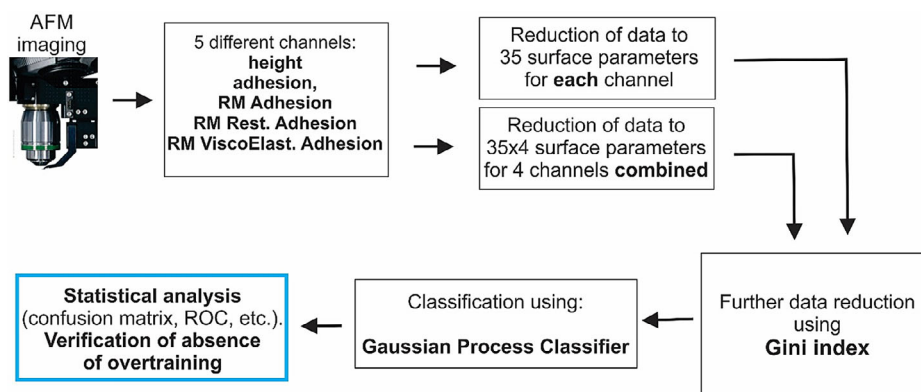


Figure 2. A schematic of data processing used in this work.

limited number of the highest ranked parameters, it is possible not only to accelerate calculations but also to increase the accuracy of classification. This is a rather typical situation because the lower ranking parameters bring essentially just noise, thereby interfering with the regression of the classifiers. In this work, we used 10 highest ranked parameters for each individual channel and 20 for the combined channels. More justification for the choice of these numbers will be given later.

The Gaussian process classifier was used as a classifier of choice. The reason was as follows. A simple prescreening of the behavior of the surface parameters demonstrates some clustering (see Figure S4, Supporting Information). One can see that clusters penetrate inside of each other. We assume Bayesian statistics for this penetration (the posterior probabilities). Therefore, it seems to be a typical case to apply the Gaussian process classifier, a nonparametric algorithm.^[38] Specifically, we used the algorithms implemented in Sklearn library. The RBF kernel and Laplace approximation were used to obtain a binary classification in this algorithm.^[39] The maximum number of iterations was chosen to be 500.

The cell indentation data are processed in a similar way. Instead of 35 surface parameters, each cell is characterized with three parameters: the effective Young's modulus, equilibrium size of the pericellular coat, and the grafting density of the pericellular brush. Five to seven indentation force curves are

analyzed per cell. The cell is assigned the values of the aforementioned three parameters. The statistical significance was found using ANOVA one-side test.

The statistical analysis of the classification was obtained as follows. We analyze the ROC curve and the confusion matrix (accuracy, specificity, and sensitivity). The ROC curve allows defining a range of sensitivity and specificity of the classification, which are defined as follows: sensitivity = TP/(TP + FN); specificity = TN/(TN + FP), where the components of the confusion matrix TP, TN, FP, and FN are true positive, true negative, false positive, and false negative, respectively. We also can calculate accuracy = (TN + TP)/(TP + FN + TN + FP). Sensitivity and specificity for a ROC point that corresponds to the minimum error of classification of both cell types while keeping the difference between sensitivity and specificity small. To find the aforementioned statistical characteristics, the entire database was split into testing and verification subsets at a predefined proportion. The testing subset was used to train the classifier, and the verification subset was used to derive all statistical parameters. This split is done randomly 1000 times. As a result, one obtains 1000 realizations of the statistical parameters. The mean values were calculated. To demonstrate the robustness of classification, we present the statistical distributions of the AUC ROC.

Finally, it is paramount to validate the absence of overtraining, which is a weak point of machine learning methods. To validate

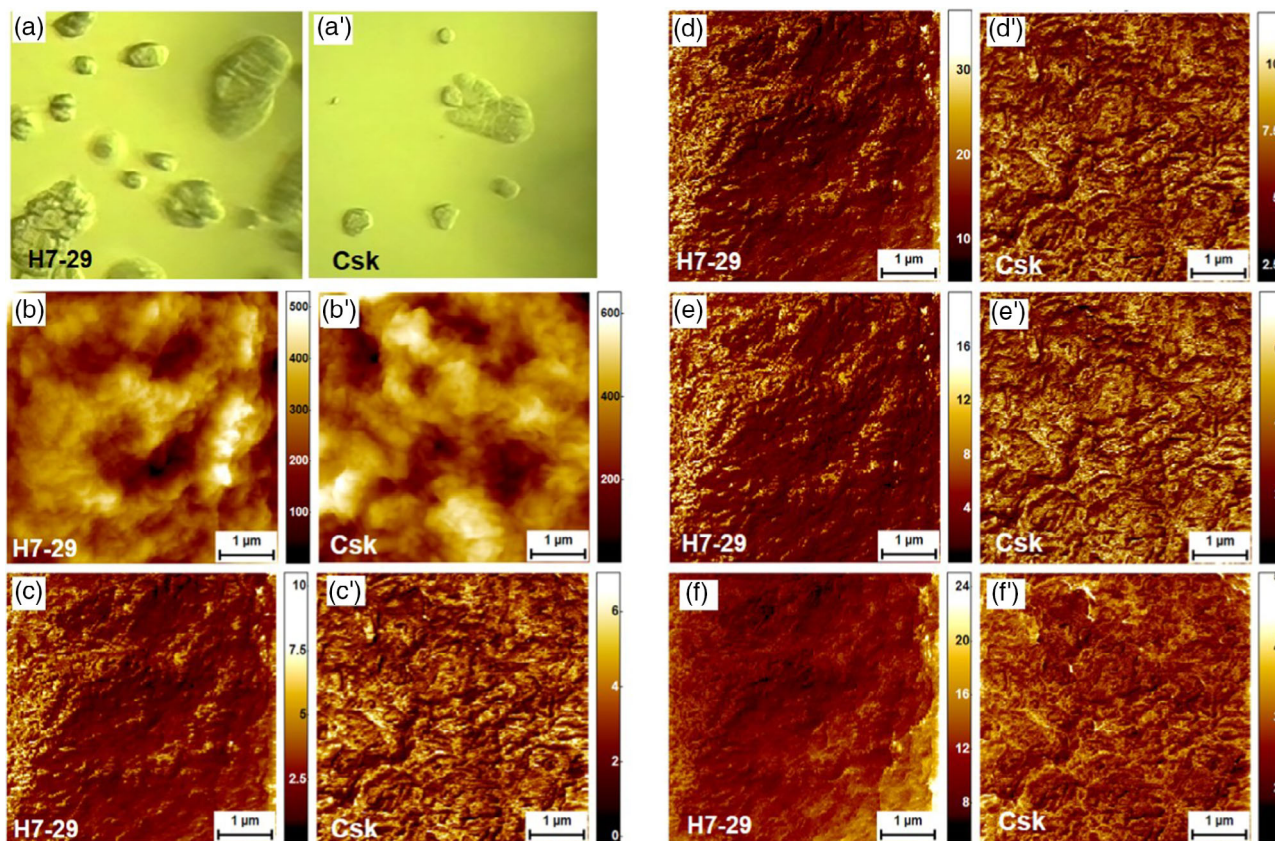


Figure 3. Representative images of cells. a,a') $350 \times 350 \mu\text{m}^2$ optical (bright-field) images of cells. b–f, b'–f') AFM images of both types of cells: b,b') height, c,c') adhesion, d,d') RM adhesion, e,e') RM restored adhesion, and f,f') RM viscoelastic adhesion of H7-29 and Csk cell lines, respectively.

our method and demonstrate the absence of any overtraining artifacts, we also use the approach described in the study by Sokolov et al.^[16] We use the same algorithms and the same data set as described earlier, but with artificially randomized class assignments (50/50% HT29 and Csk cells). If our approach lacks artifacts of training, one should see the generating of diagnostic algorithms with no classification power, i.e., close to 50% accuracy (or the AUC ROC is 0.5).

4. Experimental Results

4.1. The Analysis of AFM Images

Figure 3 shows a representative example of AFM scanning of both types of cells. Five AFM channels and regular optical bright-field images are shown. One can see in the optical images the presence of individual cells and clusters of cells. In this work,

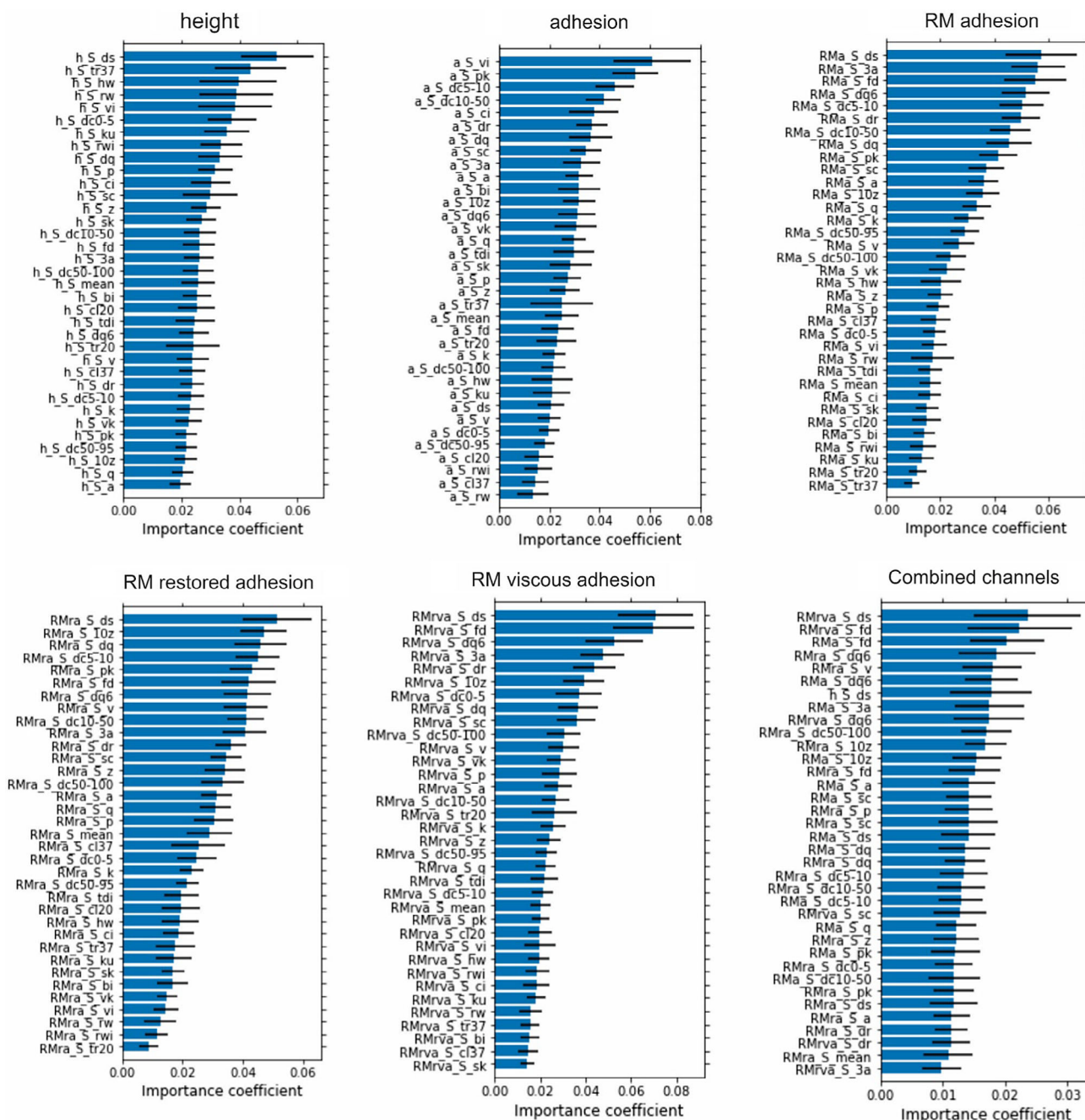


Figure 4. Gini importance index to rank the contribution of the surface parameters in the cell classification (shown as labels on the vertical axis). The average value of the index and 1 standard deviation are shown for 300 trials. The data were obtained using 29 HT29 and 24 Csk cells.

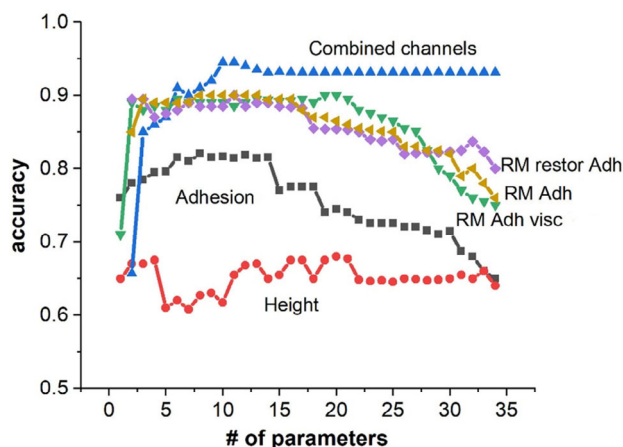


Figure 5. The result of measurements of the accuracy of classification as a function of the number of the used parameters. The values of the accuracy were calculated for 1000 random splits of the database into the training and verification subsets. The data were obtained using 29 HT29 and 24 Csk cells.

we did not differentiate between them, and collected approximately equal amount of data from both individual cells and clusters.

Although one could find differences between two types of cells, it is impossible just visually find features that are specific to one cell line or other. To differentiate these two cell lines using the recorded AFM images, we used the machine learning method described in the previous section. First, each image was reduced to 35 surface parameters. To calculate the classification accuracy of the used classifier, the database was split for training and verification (testing) subsets. There was no noticeable difference in the proportion of the split at the range between 50% and 80%; see an example of the dependence of the accuracy of classification on a particular split in Table S1, Supporting Information. Hereafter, we use 70–30% split for the training and verification subsets, respectively.

Figure 4 shows the result of the Gini importance index, which ranks features (the surface parameters) by their importance in segregation between different classes. The average value of the Gini index and 1 standard deviation are shown. These were

Table 1. The results of testing of the developed algorithms on verification subsets. The average and 1 standard deviation are shown for 1000 random splits of the database into the training and verification subsets (70–30% ratio for the size of the training in the verification subsets, respectively, was used). The data were obtained using 29 HT29 and 24 Csk cells.

Imaging channel	AUC ROC	Accuracy	Sensitivity ^{a)}	Specificity ^{a)}	Estimation of overtraining AUC/accuracy ^{b)}
Ch_h	0.64	0.60	0.56	0.60	0.45/0.46
Ch_a	0.89	0.79	0.75	0.80	0.50/0.53
Ch_RM a	0.96	0.89	0.87	0.90	0.53/0.51
Ch_RM r a	0.96	0.90	0.87	0.91	0.51/0.52
Ch_RM v a	0.96	0.89	0.89	0.90	0.57/0.52
Ch_Comb	0.99	0.94	0.90	0.93	0.46/0.45

^{a)}Sensitivity and specificity are estimated at the threshold that minimizes the error of classification (both classes). ^{b)}A possible overtraining is estimated as the AUC ROC and accuracy calculated using the same algorithm but with randomized class assignment of the data (1000 random trials).

calculated based on 300 random splits of the database for training and verification subsets. Using the highest ranked parameters, we calculate the accuracy of identification of the cell line as a function of the number of the used parameters (**Figure 5**). One can see that there is a minimum number of surface parameters that give the highest accuracy in each case. It makes sense to keep the minimum number of parameters to accelerate the computer time needed for the training. It should be noted that the minimum number of surface parameters also improves the classification based on the ROC curves. Figure S5, Supporting Information, shows the histograms of the AUC ROC for the full ($N = 35$) and reduced sets of the surface parameters. Therefore, hereafter, we used ten highest ranked parameters for each channel and 20 for the combined channels.

Comprehensive statistical results of the classification are shown in **Table 1**. In particular, the AUC ROC is shown, which is the least assumption-dependent value. It gives the probability of the classifier to separate classes. The table also presents the results for the accuracy, sensitivity, specificity, and the estimation of overtraining for each case. All results are presented for the verification subset. The estimation of the overtraining (shown as AUC ROC value) was conducted using precisely the same algorithms but processed on a database with a randomly scrambled class assignment. The complete absence of overtraining would result in an AUC ROC value equal to 0.5. The results are presented for each of five AFM imaging channels: height (h), adhesion (a), RM adhesion (RMa), RM restored adhesion (RMra), and RM viscoelastic adhesion (RMva), and one combined data (combined channels h, RMa, RMra, RMva).

Figure 6 shows the multiple ROC curves for each channel (and the combination of four channels). A 100 random splits of the database into the training and verification subsets were used (the cloud of ROC curves becomes unreadable if 1000 splits are used). The results for each individual channel as well as the combination of the channels are presented.

4.2. The Analysis of AFM Images

Here, we present the results of measurements of physical characteristics of cells, such as the effective modulus of elasticity (the Young's modulus), and parameters of the pericellular coat,

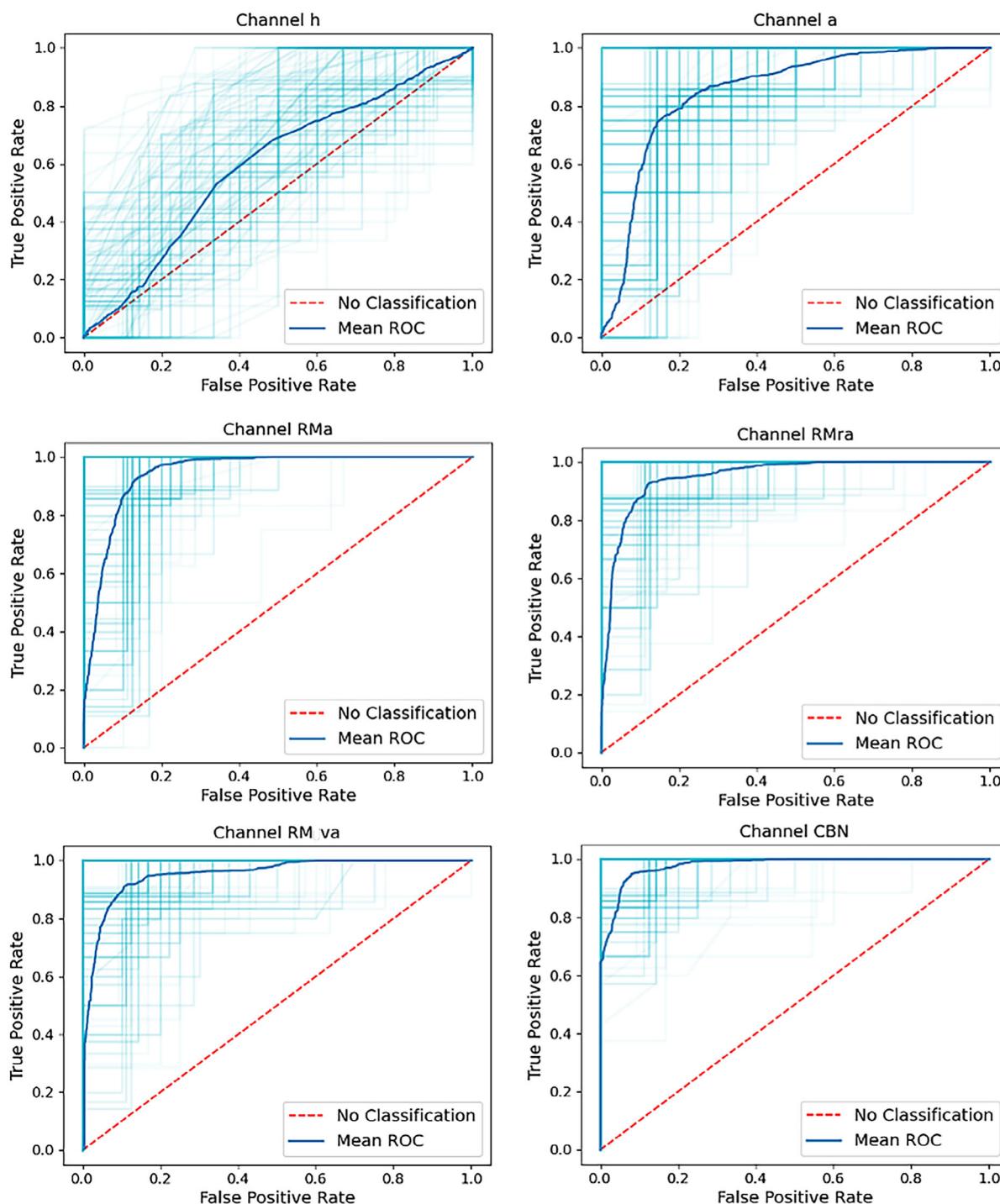


Figure 6. Clouds of ROC curves calculated for 100 random splits of the data into training and verification subsets. The average ROC curve is shown with a solid thick line. The dashed diagonal line represents no classification power. The data were obtained using 29 HT29 and 24 Csk cells.

equilibrium size of the pericellular coat, and the effective grafting density of the pericellular layer. Five to seven force curves were recorded for each of 22 H29 and 16 Csk cells. Several representative examples of the force curves are shown in Figure S6, Supporting Information. The force curves were processed through the brush model, and the results for the

physical characterization of cells are shown in **Figure 7**. The statistical distributions of the physical parameters are significantly different at the confidence level $p > 0.03$ for the elastic modulus, $p > 0.005$ for the equilibrium length of the pericellular coat, and $p > 0.04$ for the grafting density of the pericellular coat layer.

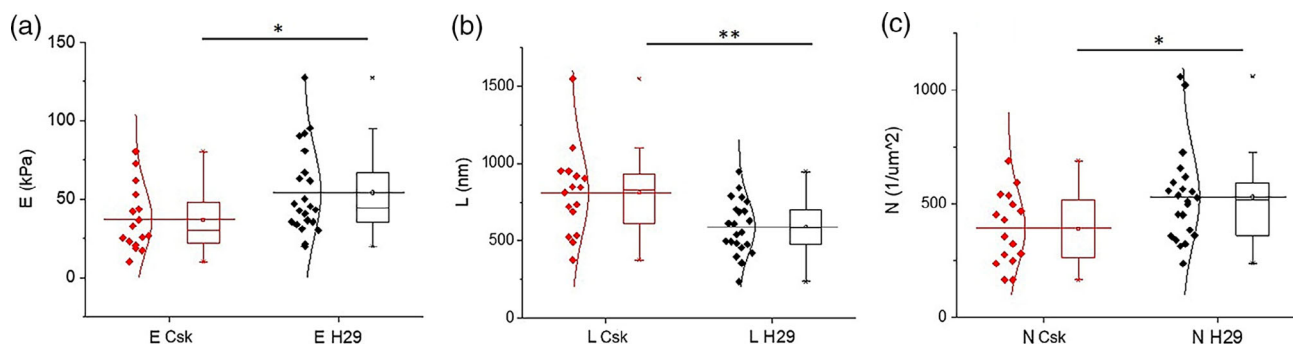


Figure 7. The results of the comparison of physical parameters of H29 and Csk cells. a) the Young's module, b) the equilibrium length of the pericellular coat, c) grafting density of the pericellular coat layer. * $p < 0.05$, ** $p < 0.005$. Five to seven force curves were recorded for each of 22 H29 and 16 Csk cells. Each point represents the average values per cell.

It should be noted that statistical significance is calculated by considering the data obtained for all cells. To find the accuracy of identification of the cell line by using a single cell, we use the same classifier, and the split 70–30% for training and verification subsets, respectively. Even combining all three physical parameters, we can get the accuracy of 68%, and the area and the ROC curve of 0.73.

5. Discussion

As we mentioned in the Introduction, the AFM indentation of cells is a traditional approach to find the difference between different cell lines, mainly between cancer lines. Therefore, it is instructional to compare the described novel approach with the traditional one. Based on the results described in the previous section, one can see that the AFM imaging gives a substantially more accurate classification of cells (94%, AUC ROC is 0.99) than the use of the traditional indentation method (68%, AUC ROC is 0.73).

It is worth noting that the traditional indentation is done on living cells. To address this potential critique, it is worth noting the following. For the purpose of comparison, the use of fixed cells seems to be appropriate because cell fixation retains the initial mechanical information.^[40] Furthermore, the most important physical parameter, the size of the pericellular layer, is comparable with the one measured on viable cells.^[2,32,41] Thus, it is conceivable to say that the size of the pericellular layer is not seriously altered by the fixation. Finally, as we mentioned in the Introduction, the use of living cells for the detection purpose is highly unlikely to be successful because of the high variation of the physical parameters of viable cells on the conditions of cell preparation.

Table 1, Figure 6, and Figure S5, Supporting Information show that the accuracy of the cell classification is substantially higher when using the RM channels. Similar to the results of the previous work,^[16] the height channel is substantially inferior compared with the adhesion channel with respect to the classification power. The accuracy based on the adhesion channel can reach 79% (AUC ROC is 0.89), whereas the accuracy of all three RM channels is 89–90% (AUC ROC is 0.96). When combining

the three RM channels and the height channel, the accuracy of classification reaches 94% (AUC ROC is 0.99).

It should be noted that the adhesion channel (of PeakForce tapping) was not included in the combined list of channels because of an excessive number of artifacts, which are shown in Figures S1–S3, Supporting Information. It should not be surprising that the artifacts are present mainly in the adhesion channel. The signal that forms the image in the height channel is recorded at the full contact of the AFM probe with the surface, where the adhesion is recorded at the moment of pull off of the AFM probe from the sample surface. The RM restored adhesion is calculated based on the free oscillation of the AFM cantilever after the pull off. The RM adhesion, however, should be quite close to the PeakForce adhesion. The observed difference is presumably due to a number of filters used in the PeakForce tapping, which may lead to some artifacts. The last RM channel, the viscoelastic adhesion channel, is just the algebraic difference between the values of RM adhesion and RM restored adhesion. It is considered here because it carries a definite physical meaning; the force difference needed to disconnect the AFM probe from the molecules of the pericellular layer. Comparing the results obtained for this channel with the other ones (Table 1, Figure 5, 6, and S2, Supporting Information), one can see that this channel brings nearly the same classification power as the other two RM channels. Thus, one can conclude that the linear combination of two channels does not increase the power of classification though the combination carries a separate well-defined physical meaning.

The sensitivity and specificity are shown in Table 1 to complete the statistical description of the classification method. One can see a relation of both sensitivity and specificity for different channels similar to the relation between accuracies described earlier. The estimation of the overtraining shows that the method is indeed almost free of overtraining, and therefore, can be considered factual.

Figure 6 and S2, Supporting Information, demonstrate the robustness of the method. One can see clustering of the ROC curves near the average values. The robustness is also seen in Figure 5, in which the accuracy is plotted for different channels of the function of the number of the top-ranking parameters used for the classification. One can see the particular robustness of the combined channels. Figure 5 shows the virtual independence of

the number of the parameters starting from ≈ 10 parameters. A very good clustering for the combined channels can be seen in both Figure 6 and S2, Supporting Information.

Finally, let us look at the question of the biophysical reason for the observed ability to segregate cells based on the machine learning analysis of the AFM images. The analysis of physical characteristics of cells, Figure 7, shows that the pericellular coat presents a statistically significant difference between the two cell lines considered in this work. Obviously, when imaging in air, the pericellular coat is collapsed. Presumably, the AFM images of the cell surface can still pick up the difference. Analyzing the Gini importance index of the surface parameters for cell separation, one can also obtain a clue about the nature of the observed difference. The most informative graph of the Gini importance indexes is the one plotted for the combined channel because it analyzes the surface parameters from all channels of interest. One can see that the top-ranked channels are S_{ds} and S_{fd} parameters. S_{ds} characterizes the “number of summits” per unit area of the sample, while the S_{fd} is the fractal dimension of the surface. Indeed, the analysis shows that S_{ds} parameter is about 10% higher for H29 cells. However, it is definitely not sufficient to classify cells. For example, Figure 5 shows that one needs to combine more than ten surface parameters to reach a high accuracy. It is interesting that the fractal dimension was a strong classifying parameter for human cervical epithelial cells.^[11,12,14,15]

6. Conclusion

Here, we used for the first time AFM RM channels combined with machine learning to identify cells from two similar but genetically modified cell lines. Using human colon cancer cell lines, HT29 cells, and Csk shRNA-transfected HT29 cells that exhibit different degrees of neoplastic aggressiveness, we demonstrated a very high classification accuracy of 94% at the level of a single cell. Analyzing the images recorded with the popular PeakForce tapping, one can see that the RM channels give higher classifying accuracy and AUC ROC: 89–90% (AUC ROC is 0.96) versus 60–79% (AUC ROC is 0.64–0.89). The traditional AFM indentation also shows statistically significant differences between the cell lines. However, the accuracy of classification of the traditional indentation method is rather modest, 68% (AUC ROC is 0.73). By multiple random splitting the entire database into testing and verification subsets, we demonstrated that the obtained results are robust, i.e., weakly dependent on the way of the splitting and the number of used parameters. All cited results were obtained on the verification subsets only. We also demonstrated the absence of overtraining of the used classifier. To conclude, the AFM cell imaging combined with machine learning could be used to identify cell phenotype at the single-cell level with a rather high precision. We expect this result will be of interest to a broad scientific community, to those who is interested in advanced imaging and machine learning, in bioinformatics, and future application of AFM in medicine.

7. Experimental Section

Cells: We leveraged paired cancer cell lines with a defined genetic modulation that is biologically significant but does not lead to morphological

and histological abnormalities detectable by diffraction-limited optical microscopy. We used human colorectal cancer cell lines, HT29 empty vector control cells, and CSK-shRNA-transfected HT29 cells. The CSK-shRNA cells were derived from the control HT29 cells by 30–50% suppression of the gene C-terminal src kinase (CSK) using RNAi. CSK is a tumor suppressor gene. Despite similar morphology, these cell variants exhibit differential neoplastic aggressiveness. CSK-shRNA cells have increased malignant aggressiveness including metastases and proliferation in animal models, as previously reported elsewhere. The cells were grown on glass slides in DMEM medium and then fixed using Karnovsky fixative using the protocol described in previous studies.^[11,42] After fixation, the cells were washed twice with PBS medium and studied with AFM working in force-volume mode.^[29] For cell imaging, fixed cells were washed in deionized (DI) water overnight and freeze-dried. To do that, a small amount of water was left on the slides, removed from DI water, and quickly frozen using a standard freeze-dryer freezer (by Labconco) for 5 min. The glass slide with the frozen sample was then placed in a freeze dryer operating in $-45\text{ }^{\circ}\text{C}$ for 1 h.

AFM: The mechanical properties of cells were studied using Dimension 3100 force microscope equipped with Nanoscope V controller (Bruker, Inc., Santa Barbara, CA) and nPoint X,Y,Z scanner (NPXY200Z25-103 by nPoint, Inc.). Five micrometer silica AFM probes were used in this study. The probes were prepared by utilizing tipless AFM cantilevers (Bruker, Inc., Santa Barbara, CA, a nominal spring constant of 0.06 N m^{-1} ; the exact spring constant was defined using thermal tuning method before gluing the silica probe) as described, e.g., in the study by Dokukin et al.^[32] Force maps (16×16 and 32×32 pixels) with a vertical ramping size of $5\text{ }\mu\text{m}$ were recorded for each cell and cell's cluster correspondingly. Vertical speed in all experiments was set to $5\text{ }\mu\text{m s}^{-1}$, allowed to record one pixel within 1.5 s. For an example of 16×16 pixels, the time of acquisition of such a map will be $16 \times 16\text{ s}$, which is a bit more than 6 min; acquisition of 32×32 pixel image will require 26 min.

The cell imaging was done by using Icon AFM equipped with Nanoscope V controller (Bruker, Inc., Santa Barbara, CA) and RM extension (NanoScience Solutions, Inc., Arlington, VA).^[43] Bruker ScanAssyst Air cantilevers were used (nominal spring constant is 0.4 N m^{-1} ; the exact spring constant was defined using thermal tuning method; the radius of curvature of the apex is $\approx 3\text{ nm}$, which can be defined using tip check samples^[23]). The probes were used until contaminated (can be good up to imaging of ≈ 100 cells). The contamination was identified by an abnormal increase in adhesion in the adhesion channel. Typically, $10 \times 10\text{ }\mu\text{m}^2$ images of the cell surface were recorded at 512×512 pixel resolution. The speed of scanning was chosen at 0.3–0.5 Hz, which is the fastest speed to have the extracted surface parameters independent of the scanning speed. Imaging of a single cell at this speed takes about 18 min.

The scanning was done in room temperature with humidity not exceeding 70% (identified as the limit for humidity-independent imaging^[11,12]). The sensitivity parameter of the photodetector was measured against a clean glass surface. The spring constants of the cantilevers were found using the thermal tuning option of Nanoscope software.

Statistical Analysis: Statistical analysis and handling of data are the essential part of the current study, which are described in the main text in detail. In brief, it is as follows: 1) preprocessing of data: row data were used without preprocessing with the exception of the height channel, which was plain fitted. The subsequent data processing is the topic of the current study, which is described in detail in the main text. 2) Data presentation: ranking of the surface parameters using Gini importance index was shown using the bar graphs for the average value and 1 standard deviation shown for 300 trials. The results of measurements of the accuracy of classification as a function of the number of used parameters were shown for multiple channels as the average accuracy calculated for 1000 random splits of the database into the training and verification subsets. The statistical results for the machine learning classifier were shown as a table for averages for the AUC ROC and the parameters of the confusion matrix; the width of the distribution of these parameters was presented as a cloud of ROC curves and histograms for the AUC ROC. The comparison of physical parameters (the Young's modulus, equilibrium length, and grafting density of the pericellular coat) was presented on the graph showing the entire distribution, Gaussian fitting, and the box graphs. 3) Sample

size for each statistical analysis: AFM force study of physical properties of cells in aqueous environment: five to seven force curves were recorded for each of 22 H29 and 16 Csk cells. Machine learning analysis of dried cells: the data were obtained using 29 HT29 and 24 Csk cells. 4) Statistical methods used to assess significant differences with sufficient details: ANOVA, one side with the confidence interval $p < 0.05$ and 0.005 . For evaluation of the results of machine learning classifier, only the testing/verification subsets were used. The evaluation of the efficiency of the machine learning classifier was done using ROC curves and the confusion matrix. 5) Software used for statistical analysis: OriginPro 2019 (ANOVA) and Python 3.1 Scikit-learn library.

Supporting Information

Supporting Information is available from the Wiley Online Library or from the author.

Acknowledgements

A.K., T.P., and P.S. contributed equally to this work. Support of this work from the National Science Foundation is acknowledged by I.S. (CMMI 1435655, CMMI 1937373). M.E.D. was partially supported by the Competitiveness Program of the National Research Nuclear University MEPhI.

Conflict of Interest

I.S. and M.E.D. are the inventors of Ringing mode, the modality used in the current study. All other authors declare no conflict of interest.

Data Availability Statement

The AFM image data are available in ASCII codes: DOI: 10.6084/m9.figshare.14336861.

Keywords

artificial intelligence, atomic force microscopy, cancer, imaging, nanomedicine

Received: December 30, 2020
Revised: March 29, 2021
Published online: May 27, 2021

- [1] P. H. Wu, D. R. B. Aroush, A. Asnacios, W. C. Chen, M. E. Dokukin, B. L. Doss, P. Durand-Smet, A. Ekpenyong, J. Guck, N. V. Guz, P. A. Janmey, J. S. H. Lee, N. M. Moore, A. Ott, Y. C. Poh, R. Ros, M. Sander, I. Sokolov, J. R. Staunton, N. Wang, G. Whyte, D. Wirtz, *Nat. Methods* **2018**, *15*, 491.
- [2] N. Guz, M. Dokukin, V. Kalaparthy, I. Sokolov, *Biophys. J.* **2014**, *107*, 564.
- [3] S. Iyer, R. M. Gaikwad, V. Subba-Rao, C. D. Woodworth, I. Sokolov, *Nat. Nanotechnol.* **2009**, *4*, 389.
- [4] N. V. Guz, S. J. Patel, M. E. Dokukin, B. Clarkson, I. Sokolov, *Nanomed-Nanotechnol.* **2016**, *12*, 2429.
- [5] N. V. Guz, S. J. Patel, M. E. Dokukin, B. Clarkson, I. Sokolov, *Nanotechnology* **2016**, *27*, 494005.
- [6] M. Lekka, P. Laidler, D. Gil, J. Lekki, Z. Stachura, A. Z. Hryniewicz, *Eur. Biophys. J.* **1999**, *28*, 312.

- [7] S. E. Cross, Y. S. Jin, J. Rao, J. K. Gimzewski, *Nat. Nanotechnol.* **2007**, *2*, 780.
- [8] S. E. Cross, Y. S. Jin, J. Tondre, R. Wong, J. Rao, J. K. Gimzewski, *Nanotechnology* **2008**, *19*, 384003.
- [9] N. Makarova, V. Kalaparthy, A. Wang, C. Williams, M. E. Dokukin, C. K. Kaufman, L. Zon, I. Sokolov, *J. Mech. Behav. Biomed.* **2020**, *107*, 103746.
- [10] M. E. Dokukin, N. V. Guz, I. Sokolov, *Jpn. J. Appl. Phys.* **2017**, *56*, 08LB01.
- [11] M. E. Dokukin, N. V. Guz, R. M. Gaikwad, C. D. Woodworth, I. Sokolov, *Phys. Rev. Lett.* **2011**, *107*, 028101.
- [12] M. E. Dokukin, N. V. Guz, C. D. Woodworth, I. Sokolov, *New J. Phys.* **2015**, *17*, 033019.
- [13] T. Berdyeva, C. D. Woodworth, I. Sokolov, *Ultramicroscopy* **2005**, *102*, 189.
- [14] N. V. Guz, M. E. Dokukin, C. D. Woodworth, A. Cardin, I. Sokolov, *Nanomed-Nanotechnol.* **2015**, *11*, 1667.
- [15] I. Sokolov, M. E. Dokukin, *Cancer Nanotechnol.: Methods Protocols* **2017**, *1530*, 229.
- [16] I. Sokolov, M. E. Dokukin, V. Kalaparthy, M. Miljkovic, A. Wang, J. D. Seigne, P. Grivas, E. Demidenko, *Proc. Natl. Acad. Sci. U. S. A.* **2018**, *115*, 12920.
- [17] A. Liu, Q. Wu, D. Peng, I. Ares, A. Anadon, B. Lopez-Torres, M. R. Martinez-Larranaga, X. Wang, M. A. Martinez, *Med. Res. Rev.* **2020**, *40*, 1973.
- [18] D. B. Asante, L. Calapre, M. Ziman, T. M. Meniawy, E. S. Gray, *Cancer Lett.* **2020**, *468*, 59.
- [19] J. Kowalik, *Prz Gastroenterol.* **2020**, *15*, 200.
- [20] A. M. McGee, D. L. Douglas, Y. Liang, S. M. Hyder, C. P. Baines, *Cell Cycle* **2011**, *10*, 4119.
- [21] D. Damania, H. Subramanian, A. K. Tiwari, Y. Stypula, D. Kunte, P. Pradhan, H. K. Roy, V. Backman, *Biophys. J.* **2010**, *99*, 989.
- [22] I. Sokolov, M. E. Dokukin, *Nanoscale Imaging: Methods Protocols* **2018**, *1814*, 469.
- [23] M. E. Dokukin, I. Sokolov, *Sci. Rep.* **2017**, *7*, 11828.
- [24] N. Makarova, B. Peng, S. Peerzade, M. E. Dokukin, I. Sokolov, *Microsc. Microanal.* **2020**, *26*, 3136.
- [25] X. F. Mallory, M. Edrisi, N. Navin, L. Nakhleh, *PLoS Comput. Biol.* **2020**, *16*, e1008012.
- [26] X. Xu, Q. Zhang, J. Song, Q. Ruan, W. Ruan, Y. Chen, J. Yang, X. Zhang, Y. Song, Z. Zhu, C. Yang, *Anal. Chem.* **2020**, *92*, 8599.
- [27] X. Zhao, S. Wu, N. Fang, X. Sun, J. Fan, *Brief Bioinform.* **2020**, *21*, 1581.
- [28] C. Ziegenhain, B. Vieth, S. Parekh, B. Reinius, A. Guillaumet-Adkins, M. Smets, H. Leonhardt, H. Heyn, I. Hellmann, W. Enard, *Mol. Cell* **2017**, *65*, 631.
- [29] I. Sokolov, V. Subba-Rao, L. A. Luck, *Biophys. J.* **2006**, *90*, 1055.
- [30] I. Sokolov, S. Iyer, V. Subba-Rao, R. M. Gaikwad, C. D. Woodworth, *Appl. Phys. Lett.* **2007**, *91*, 023902.
- [31] I. Sokolov, M. E. Dokukin, *Nanoscale Imaging: Methods Protocols* **2018**, *1814*, 469.
- [32] M. Dokukin, Y. Ablaeva, V. Kalaparthy, A. Seluanov, V. Gorbunova, I. Sokolov, *Biophys. J.* **2016**, *111*, 236.
- [33] H. J. Butt, M. Kappl, H. Mueller, R. Raiteri, W. Meyer, J. Ruhe, *Langmuir* **1999**, *15*, 2559.
- [34] S. Iyer, R. M. Gaikwad, V. Subba-Rao, C. D. Woodworth, I. Sokolov, *Nat. Nanotechnol.* **2009**, *4*, 389.
- [35] I. Sokolov, S. Iyer, V. Subba-Rao, R. M. Gaikwad, C. D. Woodworth, *Appl. Phys. Lett.* **2007**, *91*, 023902.
- [36] F. E. Harrell, Jr., K. L. Lee, R. M. Califf, D. B. Pryor, R. A. Rosati, *Stat. Med.* **1984**, *3*, 143.

- [37] Y. i. Anzai, *Pattern Recognition and Machine Learning*, Academic Press, Boston **1992**.
- [38] C. E. Rasmussen, C. K. I. Williams, *Gaussian Processes for Machine Learning*, MIT Press, Cambridge, MA. **2006**.
- [39] C. K. I. Williams, D. Barber, *IEEE Trans. Pattern Anal.* **1998**, *20*, 1342.
- [40] S. O. Kim, J. Kim, T. Okajima, N. J. Cho, *Nano Conver.* **2017**, *4*, 5.
- [41] M. Simon, M. Dokukin, V. Kalaparthi, E. Spedden, I. Sokolov, C. Staii, *Langmuir* **2016**, *32*, 1111.
- [42] P. M. Echols-Jones, M. E. Dokukin, I. Sokolov, W. C. Messner, in *Proc. of the ASME 9th Annual Dynamic Systems and Control Conf.*, Vol. 1, Minneapolis, MI **2017**.
- [43] M. E. Dokukin, I. Sokolov, *Sci. Rep.* **2017**, *7*, 11828.